Supplemental Information

Tuning Nanoparticle Interactions with Ovarian Cancer through Layer by Layer Modification of Surface Chemistry

*Santiago Correa[a,i], Natalie Boehnke[b], Antonio E. Barberio[d], Elad Deiss-Yehiely[c], Aria Shi[a], Benjamin Oberlton[a], Sean G. Smith[b,d], Ioannis Zervantonakis[f,ii], Erik C. Dreaden[b,iii], Paula T. Hammond[b,d,e]**

[a]Department of Biological Engineering, Massachusetts Institute of Technology, 21 Ames Street, Cambridge, MA 02142, USA

[b]Koch Institute for Integrative Cancer Research, Massachusetts Institute of Technology, 500 Main Street, Cambridge, MA 02142, USA

[c]Department of Materials Science and Engineering, Massachusetts Institute of Technology, 183 Memorial Drive, Cambridge, MA 02142, USA

[d]Department of Chemical Engineering, Massachusetts Institute of Technology, 25 Ames Street, Cambridge, MA 02142, USA

[e]Institute for Soldier Nanotechnologies, Massachusetts Institute of Technology, 500 Technology Square, Cambridge, MA 02139, USA

[f]Department of Cell Biology, Ludwig Center at Harvard, Harvard Medical School, Boston, MA, 02115, USA

*Corresponding author

Present Addresses

[i]Materials Science and Engineering, Stanford University, 496 Lomita Mall, CA 94305

[ii]Department of Bioengineering, University of Pittsburgh, 302 Benedum Hall, 3700 O'Hara Street, Pittsburgh, PA, 15260

[iii]Coulter Department of Biomedical Engineering, Georgia Institute of Technology and Emory University, 1760 Haygood Drive, Atlanta, GA 30322
Department of Pediatrics, Winship Cancer Institute, Emory University, 201 Dowman Dr, Atlanta, GA 30322
Petit Institute for Bioengineering and Bioscience, Georgia Institute of Technology, 315 Ferst Dr NW, Atlanta, GA 30332
Aflac Cancer and Blood Disorders Center, Children's Healthcare of Atlanta and Emory School of Medicine, 1405 Clifton Rd, Atlanta, GA 30322

Supplemental discussion of live-cell imaging results with the LbL-NP panel

Consistent with our prior studies, COOH-LbL-NPs accumulated significantly in JHOS4 cells during the twenty-four hour incubation (**Figure S3**), while SO_3-LbL-NPs and CML-NPs were poorly associated with cancer cells. Again, COOH-LbL-NPs without a known targeting ligand (PLD-NPs, PLE-NPs, poly(ethylene glycol-b-poly-L-glutamate (PEG-b-PLE)-NPs, PAA-NPs) were significantly associated with the cell membrane at twenty-four hours. PEG-b-PLE-NPs and PAA-NPs were almost exclusively limited to the cell surface. PLE-coated NPs had a small endolysosomal fraction, while PLD-coated NPs had both a significant surface-bound and endolysosomal fraction. Consistent results were also seen in the COV362 and Caov3 lines with select formulations (**Figures S4 and S5**). HA-coated NPs were almost entirely intracellular at this time point. The SO_3-LbL-NPs were generally internalized – with the exception of fucoidan-coated particles which appear primarily on the surface of JHOS4 cells. Inclusion of folate on HF-NPs appears to improve accumulation in perinuclear vesicles, relative to the parental HS-NP formulation. CML-NPs, while less abundant, are also generally internalized. With the exception of HA-NPs, the live-cell imaging results suggest a shared ability for COOH-LbL-NPs to associate with cell membranes for prolonged periods of time.

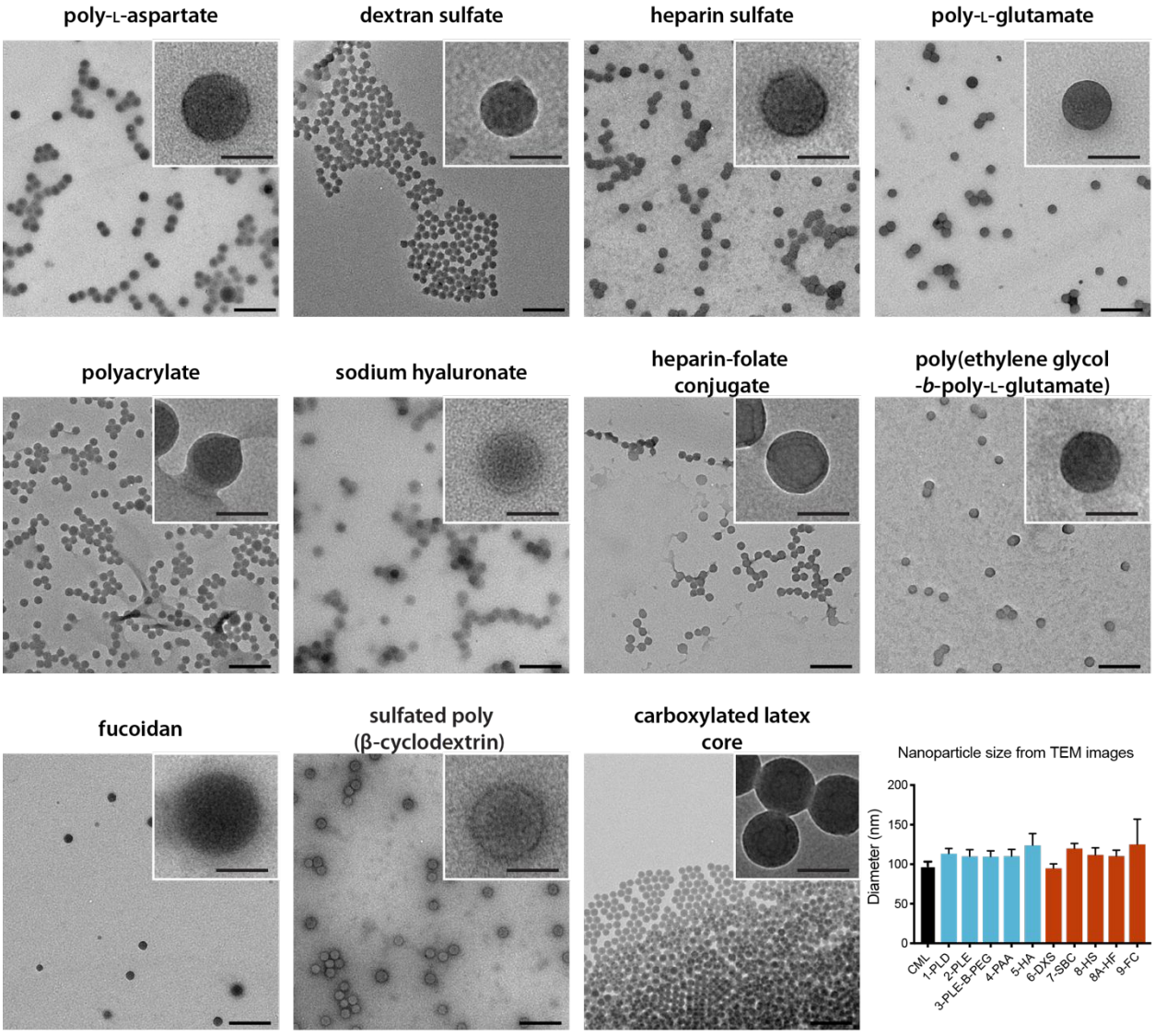

Figure S1. Transmission electron microscopy was performed on all nanoparticle formulations, revealing uniform particle populations with approximately 100 nm diameters. Specimens were drop-casted from a 10 µg/mL solution onto a mesh copper grid coated with a continuous carbon film and then imaged on a JEOL 2011 High Contrast Digital TEM (120 kV). The scale bar in the low-magnification image denotes 500 nm and the scale bar for the insets represents 100 nm. Particle size was measured using built-in functionality in the open-source software FIJI.

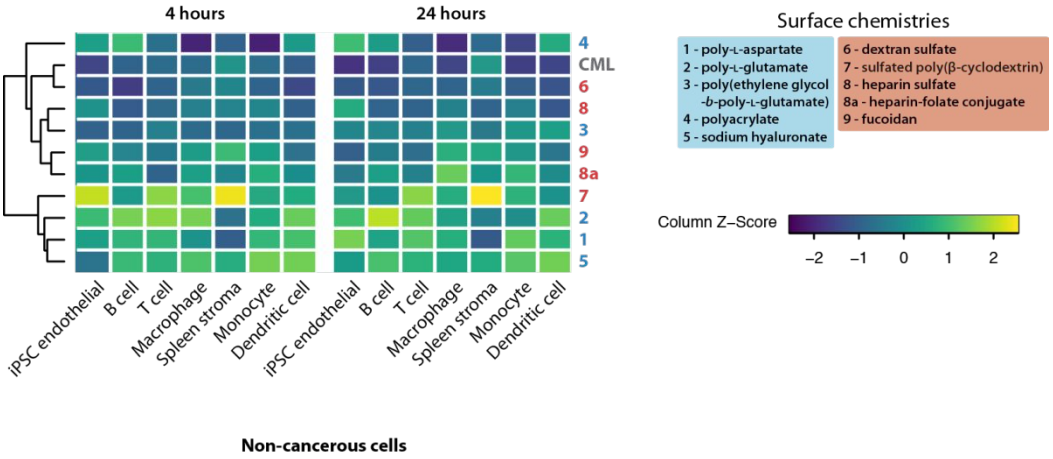

Figure S2. Hierarchical clustering of nanoparticle binding data from flow cytometry experiments on noncancerous cells. The clusters identified do not correspond to surface chemistry, in contrast to clustering results in cancer cells shown in Figure 2.

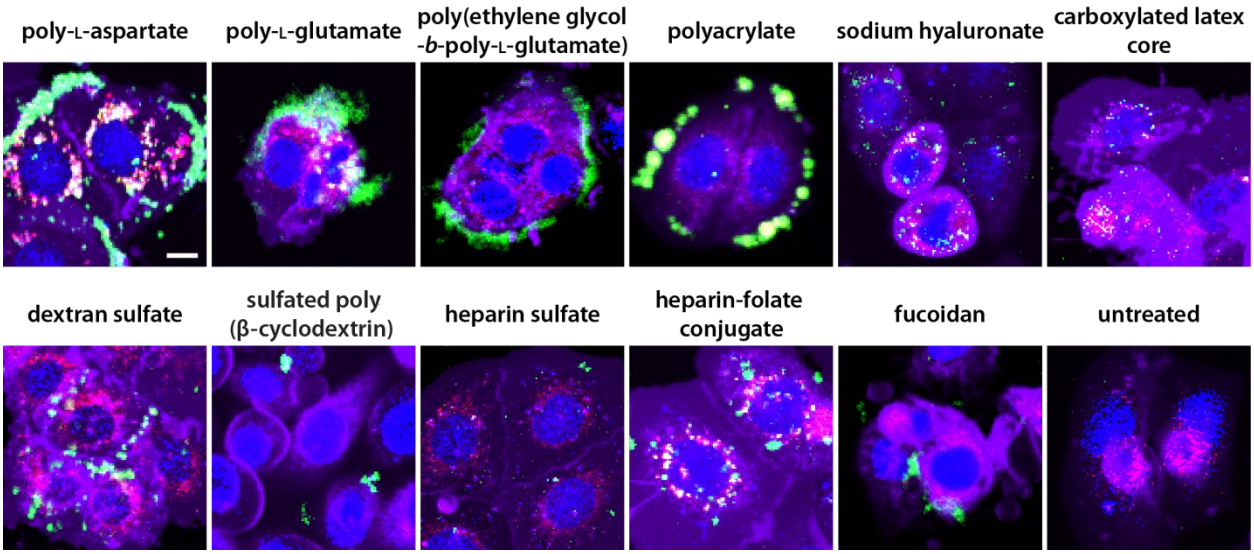

Figure S3. Live-cell imaging reveals that individual LbL-NP formulations mediate distinct subcellular trafficking. JHOS4 ovarian cancer cells were incubated with 20 pM concentrations of LbL-NPs and imaged live using a confocal microscope. Consistent with flow cytometry results, carboxylated LbL-NPs bind JHOS4 cells more efficiently than sulfated formulations. The JHOS4 cells appear to traffic individual carboxylated formulations differently, sometimes accumulating particles on the surface in the case of poly-L-glutamate or internalizing them efficiently in the case of sodium hyaluronate. Inclusion of the folate on the heparin sulfate-coated system provides enhances accumulation and internalization relative to the corresponding heparin sulfate NP. Nanoparticle signal shown in green, lysotracker signal shown in red, cell membrane shown in magenta, nuclei shown in blue. Scale bar in the first micrograph denotes 10 μm for all images.

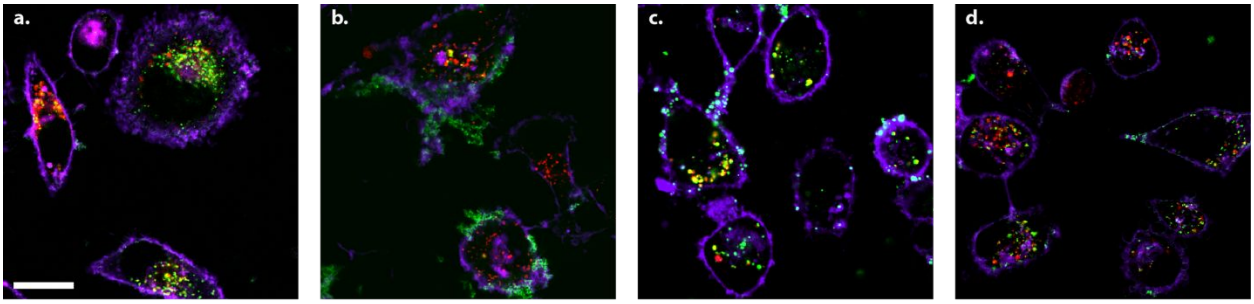

Figure S4. Live-cell imaging of COV362 ovarian cancer cells reveal consistent subcellular localization for key LbL-NPs. Cells were incubated with 20 pM concentrations of LbL-NPs and imaged live using a confocal microscope. **a)** HA-NPs were observed internalized by cells. **b)** PLE-NPs again demonstrated surface coating morphology with limited penetration into the cell. **c)** The PLD-NPs appeared as punctate signals from within the cells and on the membrane and cellular projections. **d)** HF-NPs were mostly internalized at this time point, but were less abundant relative to the carboxylated LbL-NPs. Nanoparticle signal shown in green, lysotracker signal shown in red, and cell membrane shown in magenta. Scale bar in the first micrograph denotes 10 μm for all images.

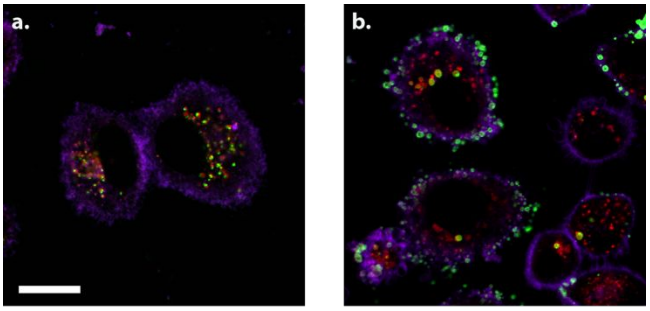

Figure S5. Live cell imaging of Caov3 ovarian cancer cells also reveals consistent subcellular localization of HA and PLD-NPs. Cells were incubated with 20 pM concentrations of LbL-NPs and imaged live using a confocal microscope. **a)** HA-coated NPs are internalized and organized inside or near lysosomes. **b)** PLD-coated LbL NPs are observed as punctate spots on the membrane surface as well as co-localized with lysosomes. Nanoparticle signal shown in green, lysotracker signal shown in red, and cell membrane shown in magenta. Scale bar in the first micrograph denotes 10 μm for both images.

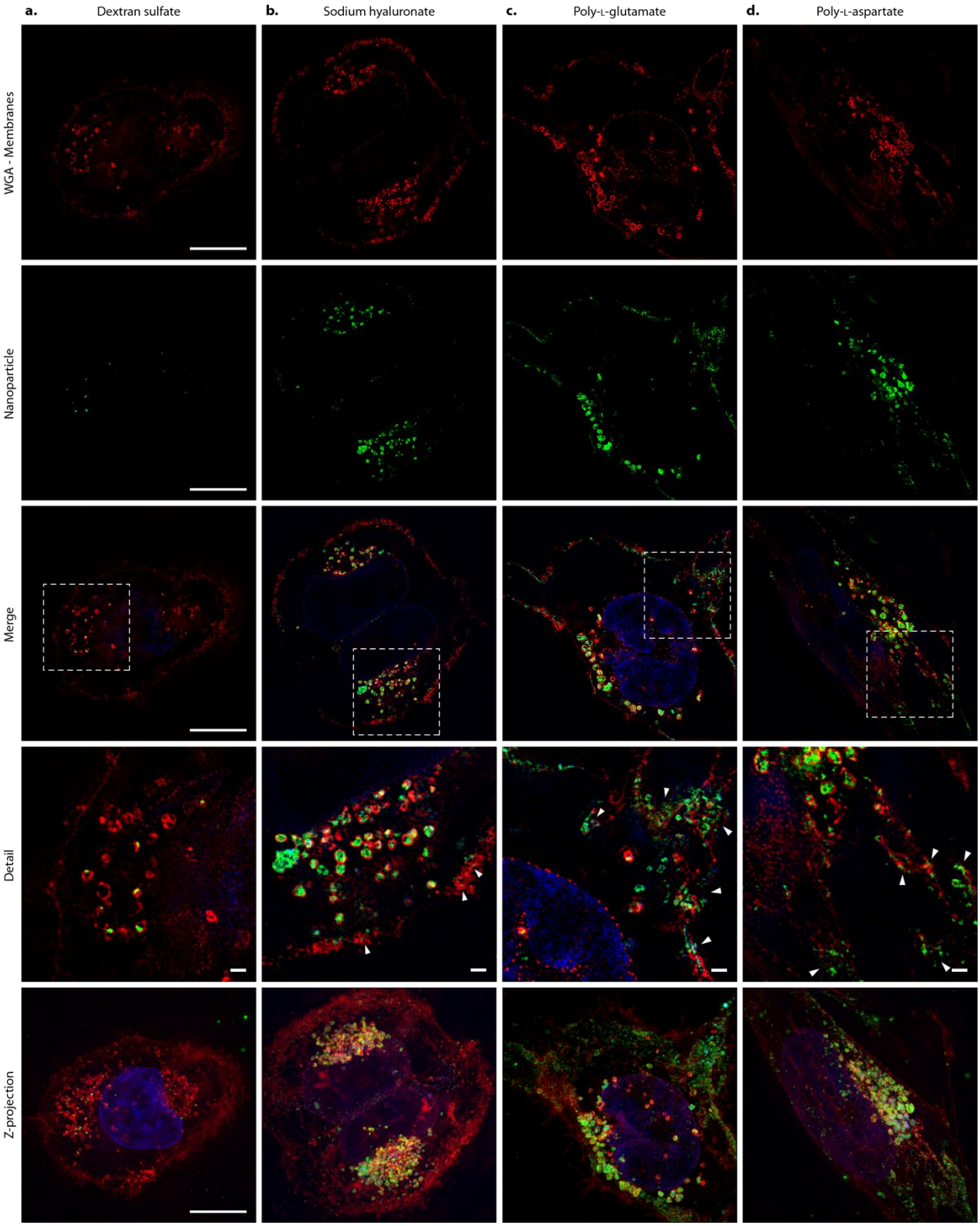

Figure S6. Surface chemistry on LbL NPs shapes subcellular fate and influences the partitioning of NPs on the membrane and on the interior of OVCAR8 cells. Cells were treated with 4 pM LbL NP for 24 hours and then fixed and processed for super resolution microscopy. Wheat germ agglutinin (WGA) was used to stain membranes

(including outer membrane, vesicular membranes and the nuclear membrane) and is shown in red. Nanoparticles are shown in green and nuclei in blue. Scale bars denote 10 microns, with the exception of the scale bar for the detail panels, where they denote 1 micron. **a)** DXS-NPs are observed on the interior of the cell within vesicular structures. **b)** HA-NPs are found in enlarged vesicles within the cell, but also in small punctate spots on the membrane surface as indicated with white arrows. **c)** PLE-NPs are observed inside enlarged vesicles, but with a considerable fraction on the membrane with a seemingly diffuse morphology as indicated by the arrows. **d)** PLD-NPs are found both inside enlarged vesicles and on the membrane. However, PLD-NPs on the membrane appear more as punctate structures as indicated by arrows in the detail row.

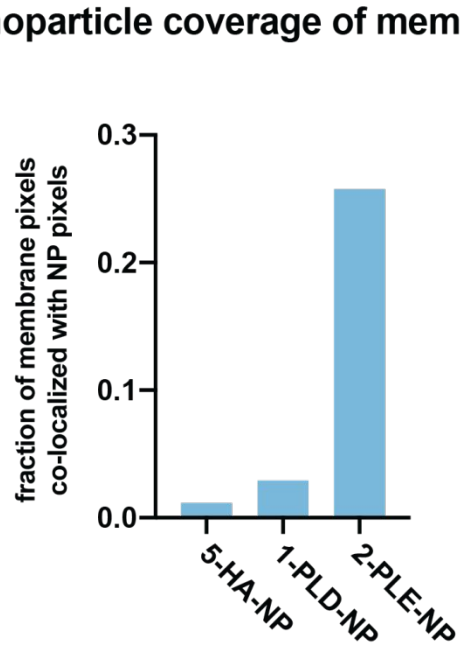

Figure S7. Co-localization of nanoparticle and extracellular membrane. Super-resolution images from Figure 4a were used to determine the fraction of membrane pixels co-localized with nanoparticle pixels.

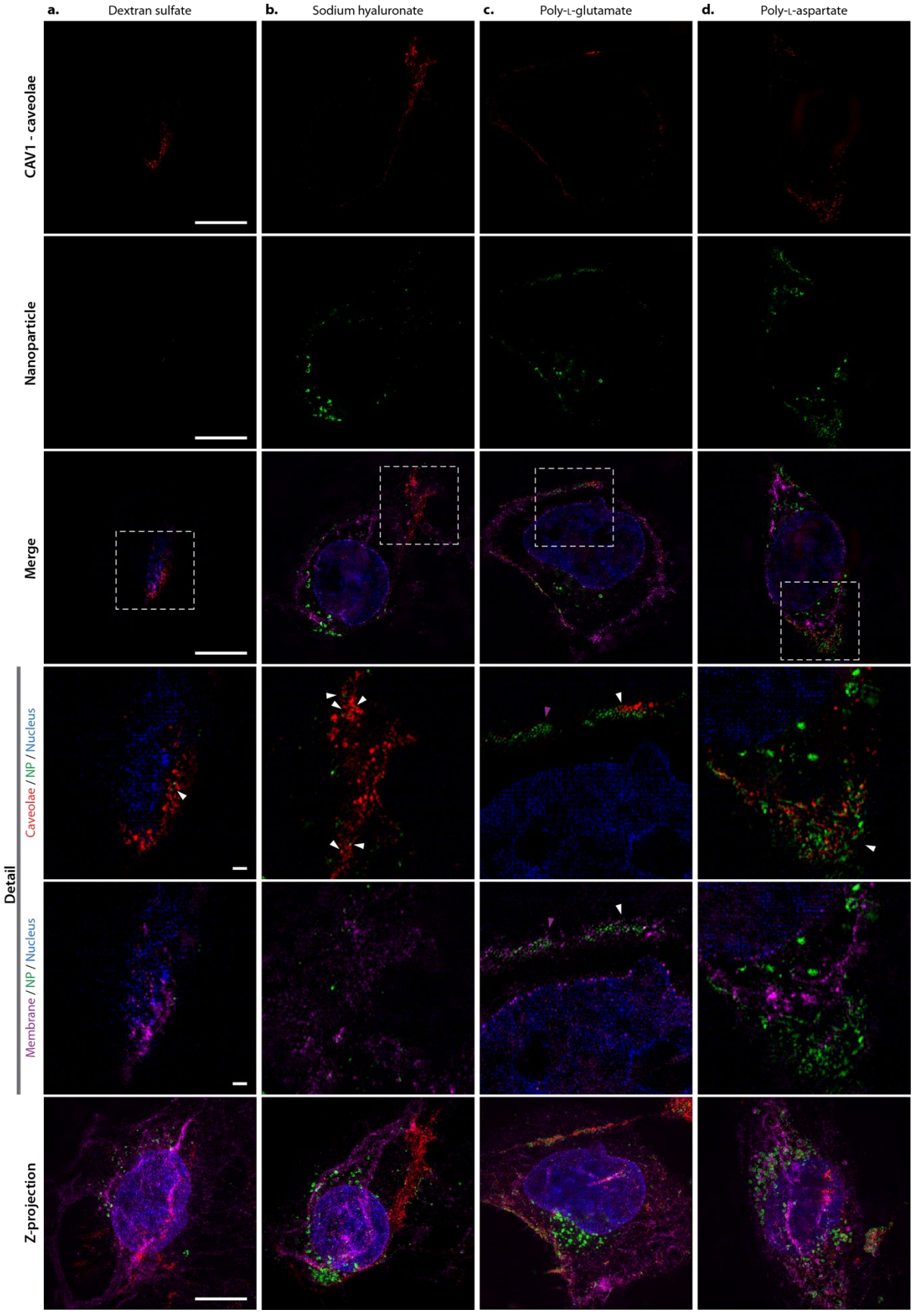
a. Dextran sulfate
b. Sodium hyaluronate
c. Poly-L-glutamate
d. Poly-L-aspartate
CAV1 - caveolae
Nanoparticle
Merge
Detail
Caveolae / NP / Nucleus
Membrane / NP / Nucleus
Z-projection

Figure S8. Surface bound LbL-NPs differ with regard to their interaction with caveolae at 24 hours in OVCAR8 cells. Cells were treated with 4 pM LbL NP for 24 hours and then fixed and processed for super resolution microscopy. CAV1 proteins are stained to label the caveolar compartment, and are shown in red. Wheat germ agglutinin (WGA) was used to stain membranes (including outer membrane, some vesicular membranes and the nuclear membrane) and is shown in magenta. Nanoparticles are shown in green and nuclei in blue. Scale bars denote 10 microns, with the exception of the scale bar for the detail panels, where they denote 1 micron. **a)** Although almost entirely internalized, some faint DXS-NP signal was noted near a patch of caveolae. **b)** Rare surface-bound fractions of HA-NPs were associated with caveolae. **c)** Most surface-bound PLE-NPs are not associated with caveolae as indicated by the purple arrow. **d)** Most surface-bound PLD-NP are generally associated with the caveolar compartment.

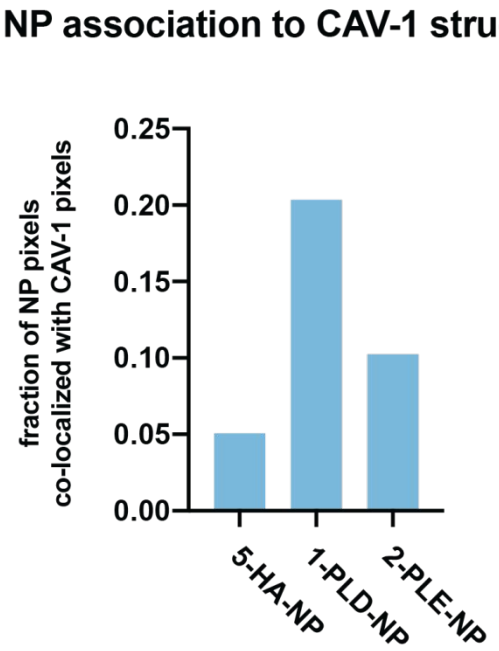

Figure S9. Co-localization analysis of nanoparticles and CAV-1. Super-resolution images in Figure 4b were analyzed to determine the fraction of nanoparticle pixels overlapped with CAV-1 pixels.

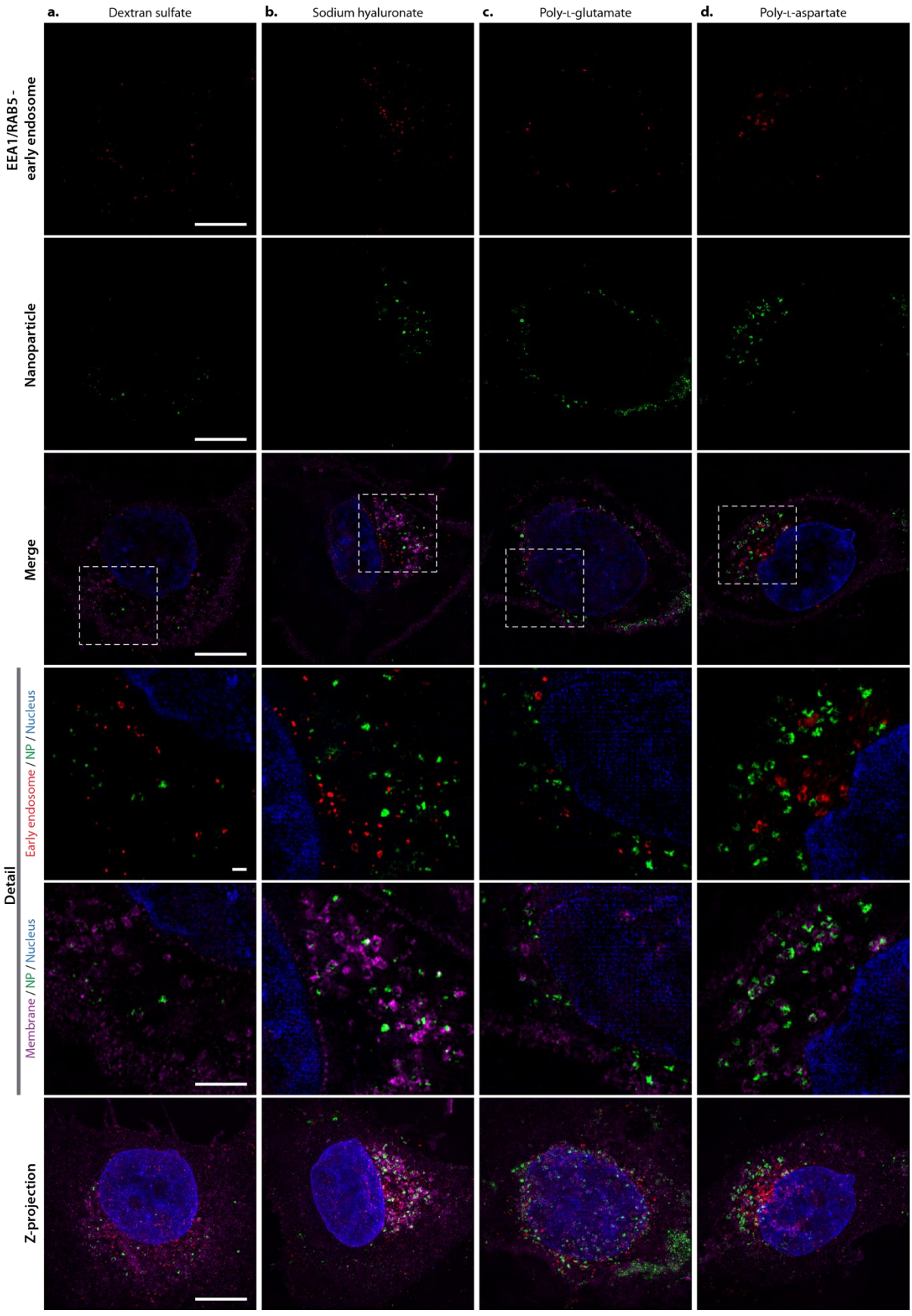
a. Dextran sulfate
b. Sodium hyaluronate
c. Poly-L-glutamate
d. Poly-L-aspartate
EEA1/RAB5 - early endosome
Nanoparticle
Merge
Detail
Early endosome / NP / Nucleus
Membrane / NP / Nucleus
Z-projection

Figure S10. By 24 hours, LbL NPs do not appear to co-localize with early endosomal compartments. Cells were treated with 4 pM LbL NP for 24 hours and then fixed and processed for super resolution microscopy. EEA1 and Rab5 proteins are stained to label the early endosomal compartments, and are shown in red. Wheat germ agglutinin (WGA) was used to stain membranes (including outer membrane, some vesicular membranes and the nuclear membrane) and is shown in magenta. Nanoparticles are shown in green and nuclei in blue. Scale bars denote 10 microns, with the exception of the scale bar for the detail panels, where they denote 1 micron.

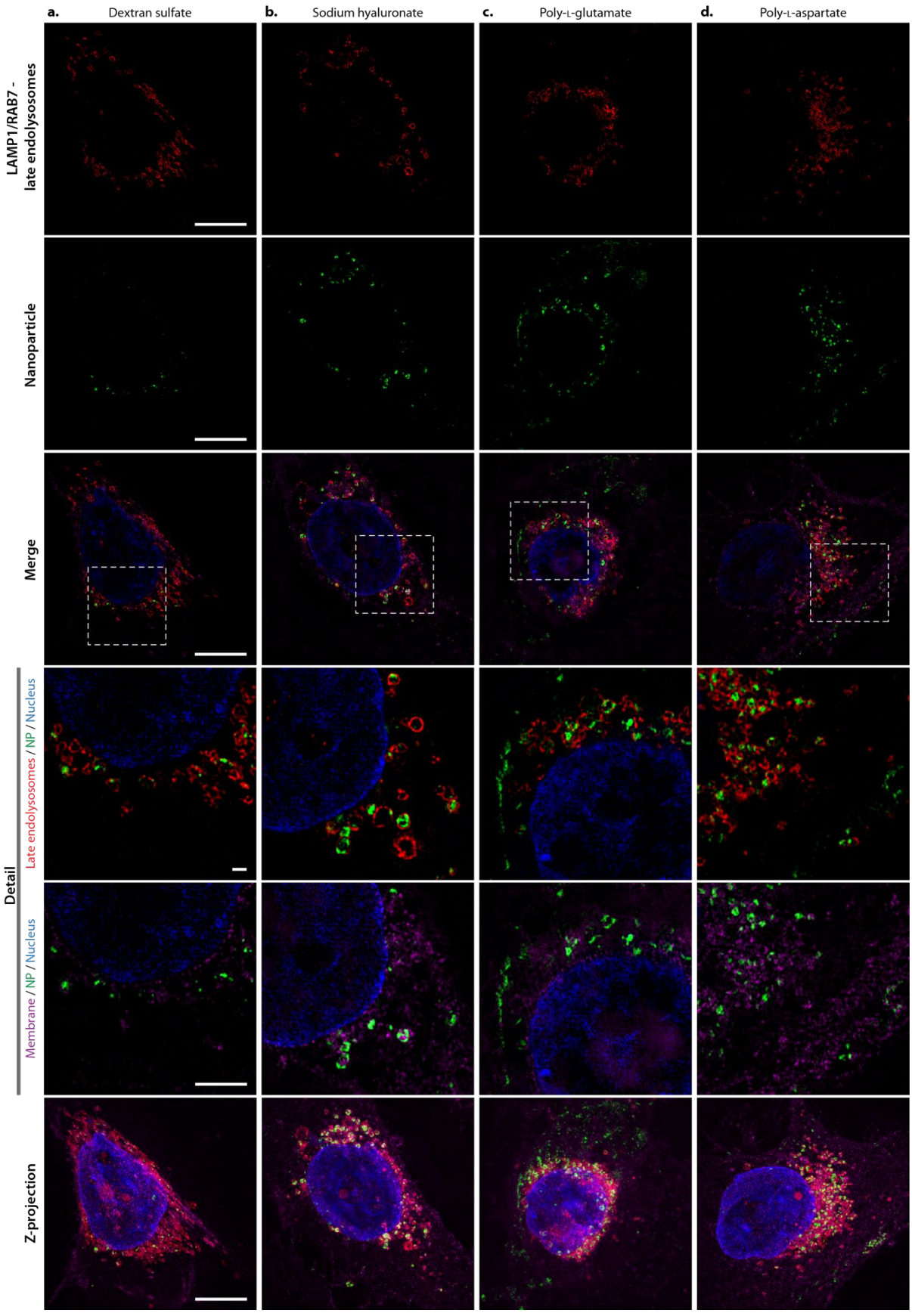
a. Dextran sulfate
b. Sodium hyaluronate
c. Poly-L-glutamate
d. Poly-L-aspartate
LAMP1/RAB7 - late endolysosomes
Nanoparticle
Merge
Detail
Late endolysosomes / NP / Nucleus
Membrane / NP / Nucleus
Z-projection

Figure S11. Internalized LbL NPs navigate to the late endolysosomal compartment in OVCAR8 cells. Cells were treated with 4 pM LbL NP for 24 hours and then fixed and processed for super resolution microscopy. LAMP1 and Rab7 proteins are stained to label the lysosomal and late endosomal compartments, and are shown in red. Wheat germ agglutinin (WGA) was used to stain membranes (including outer membrane, some vesicular membranes and the nuclear membrane) and is shown in magenta. Nanoparticles are shown in green and nuclei in blue. Scale bars denote 10 microns, with the exception of the scale bar for the detail panels, where they denote 1 micron. All internalized NPs appear to be contained within this compartment at this time point.

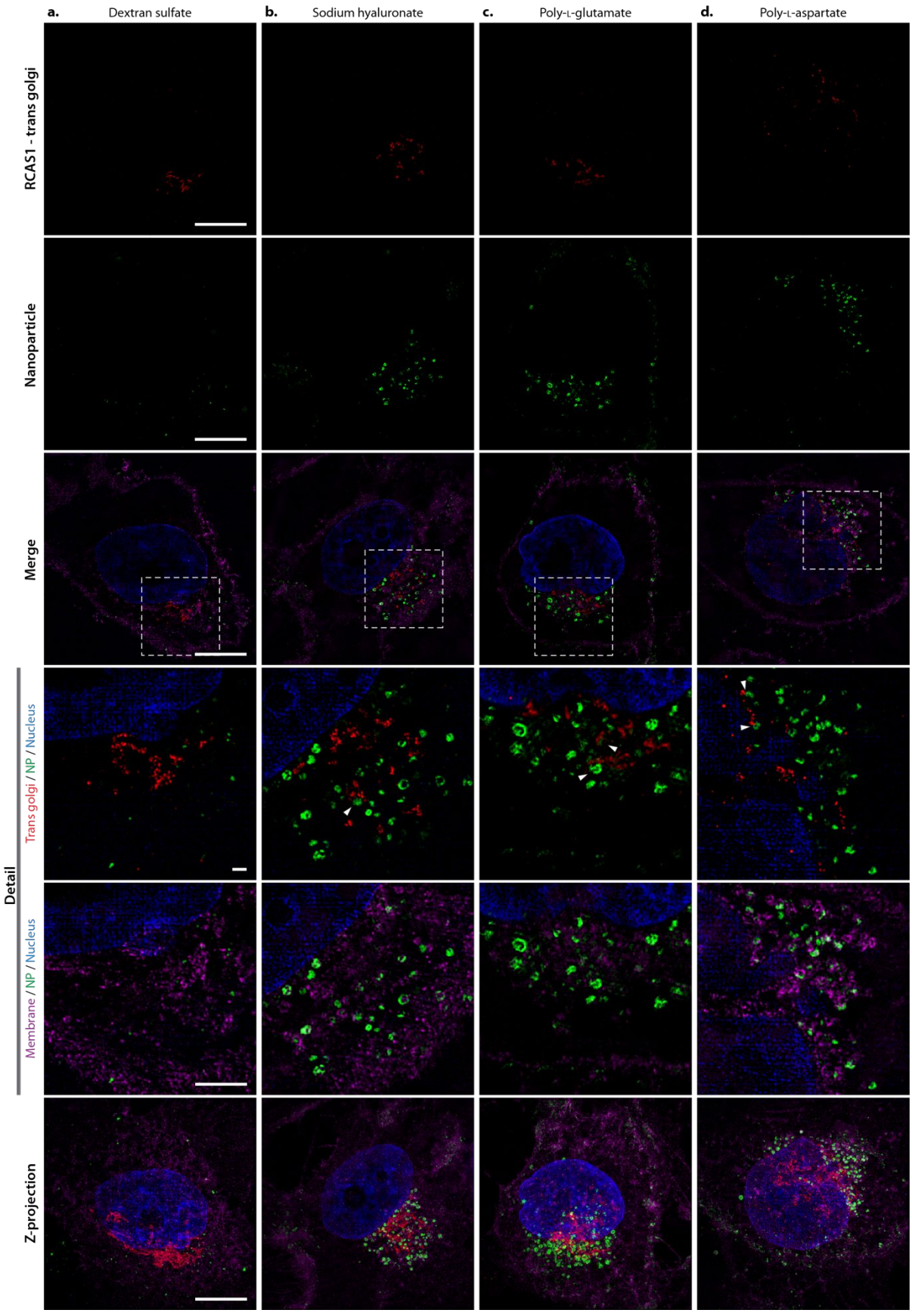
a. Dextran sulfate
b. Sodium hyaluronate
c. Poly-L-glutamate
d. Poly-L-aspartate
RCAS1 - trans golgi
Nanoparticle
Merge
Detail
Trans golgi / NP / Nucleus
Membrane / NP / Nucleus
Z-projection

Figure S12. Carboxylated LbL-NPs can be found near and in between trans golgi stacks, but not inside them. Cells were treated with 4 pM LbL NP for 24 hours and then fixed and processed for super resolution microscopy. RCAS1 proteins are stained to label the trans golgi compartment, and are shown in red. Wheat germ agglutinin (WGA) was used to stain membranes (including outer membrane, some vesicular membranes and the nuclear membrane) and is shown in magenta. Nanoparticles are shown in green and nuclei in blue. Scale bars denote 10 microns, with the exception of the scale bar for the detail panels, where they denote 1 micron. a) Dextran sulfate-coated NPs do not appear in close proximity to the trans golgi, though this may be a function of overall amount of NP in the cell. b-d) Sodium hyaluronate, poly-L-glutamate, and poly-L-aspartate-coated NPs are observed near golgi stacks, sometimes in very close proximity as denoted by the arrows.

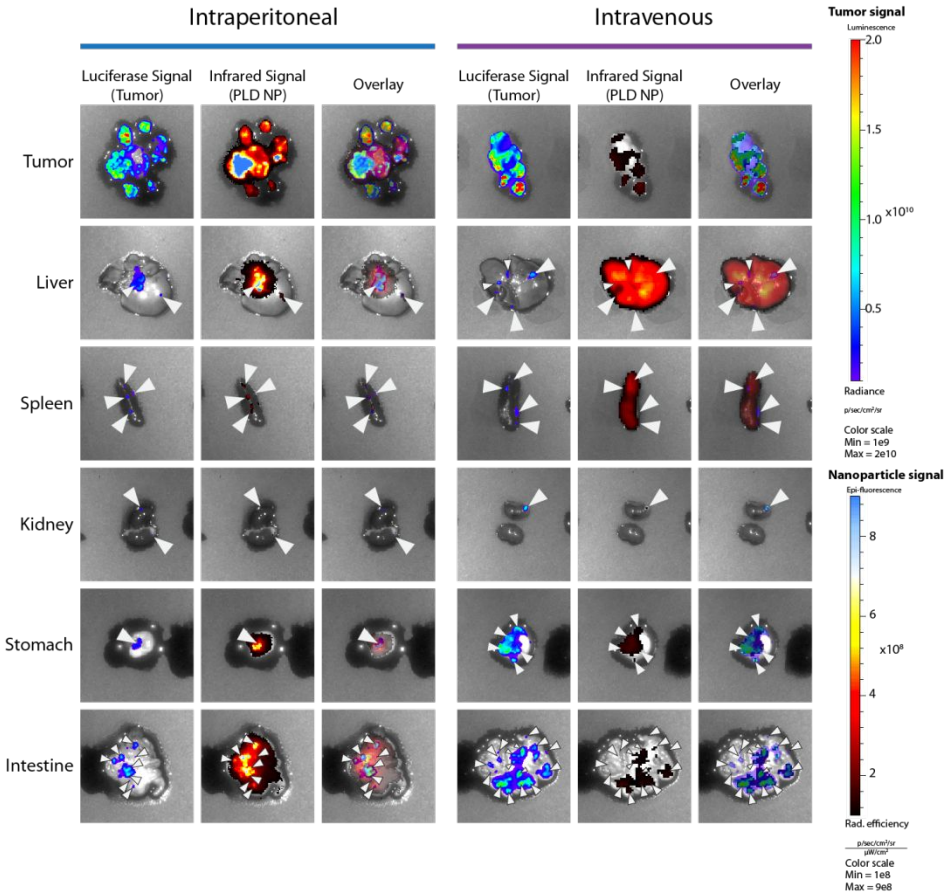

Figure S13. Biodistribution of PLD-coated LbL NPs at 24 hours after either IV or IP-administration. Luciferase signal from tumor cells and infrared fluorescence from nanoparticles were measured for each organ using an IVIS instrument. Arrows denote metastases on organs. IV administration of PLD NPs led to diffuse signal in the liver and spleen, indicating removal by these filtration organs. Co-localization of NP with the metastatic nodules of the intestine and stomach indicate tumor-homing ability. IP-administered PLD-NPs appear to be present throughout the primary tumor and in all detectable metastatic nodules in the other IP organs.

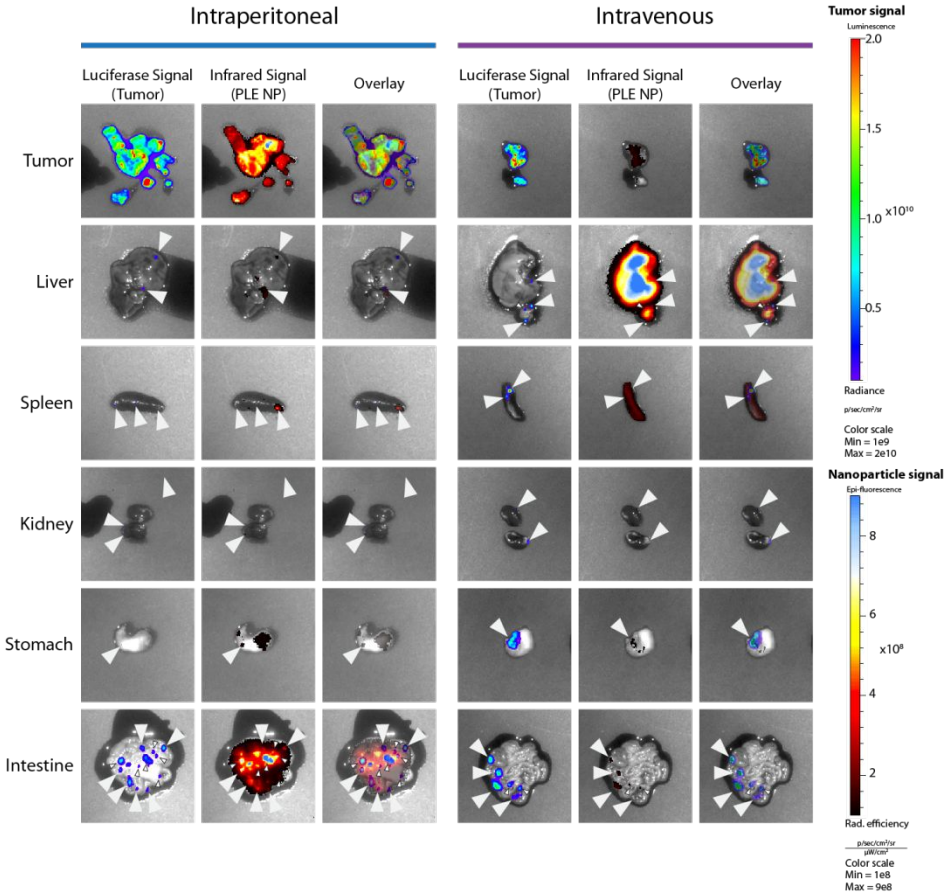

Figure S14. PLE-NP biodistribution at 24 hours after either IV or IP-administration. Luciferase signal from tumor cells and infrared fluorescence from nanoparticles were measured for each organ using an IVIS instrument. Arrows denote metastases on organs. IV-administration of PLE-NPs led to accumulation in the liver and spleen. More NP signal is detected from tumors of IP-administered mice. Co-localization of PLE-NP with metastases on the intestine were noted in the IP-administered model.

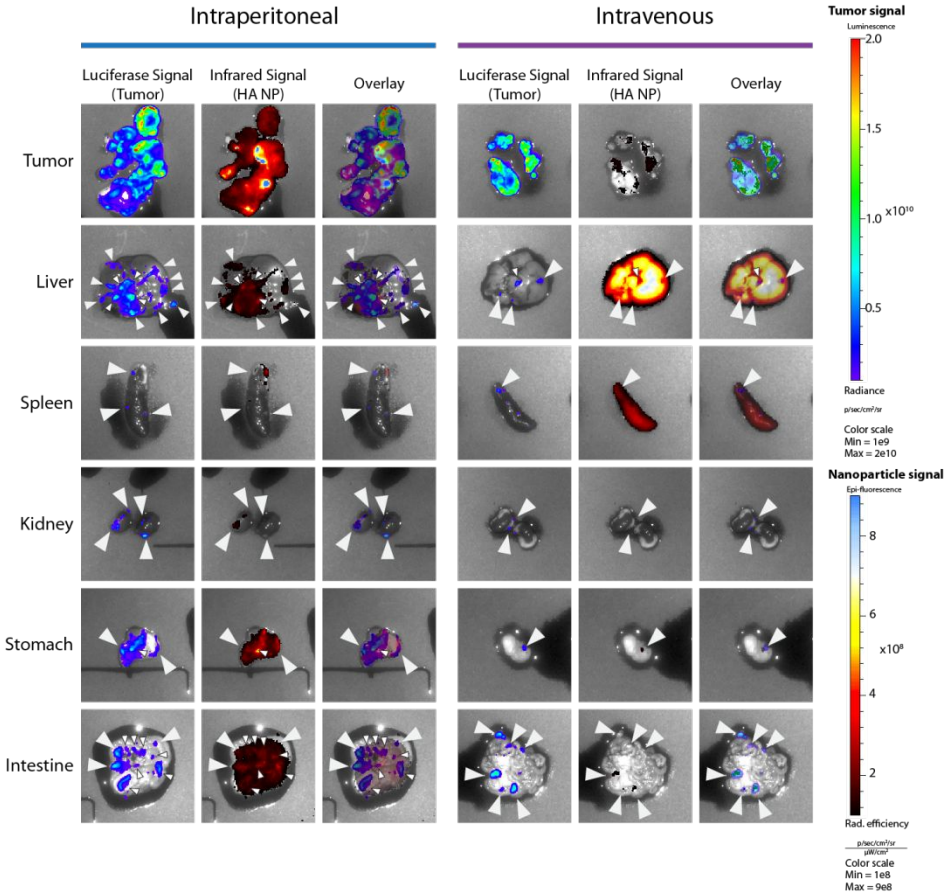

Figure S15. HA-NP biodistribution 24 hours after either IP or IV administration. Luciferase signal from tumor cells and infrared fluorescence from nanoparticles were measured for each organ using an IVIS instrument. Arrows denote metastases on organs. Both IV and IP-administered NPs appear to co-localize with several of the metastatic lesions on the stomach and intestine. The majority of the IV dose appears to accumulate in the liver and spleen. IP-administered HA NPs were observed to accumulate throughout the primary tumor as well as the majority of the malignant lesions throughout the IP cavity.

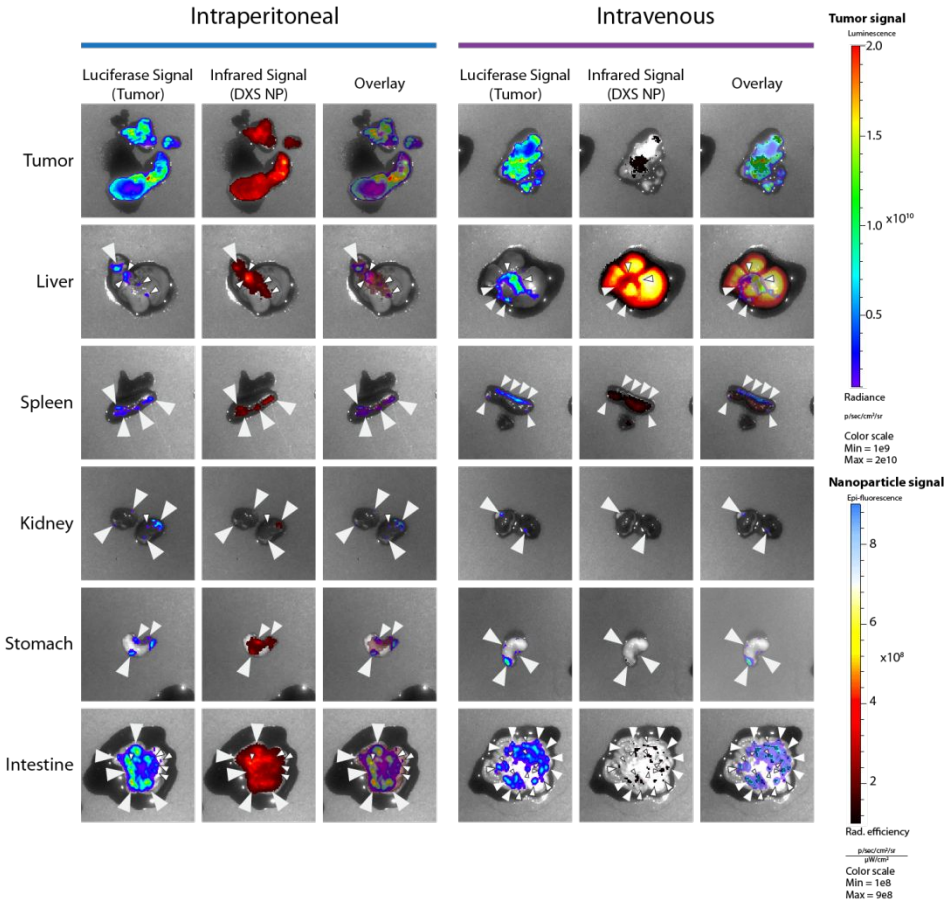

Figure S16. The biodistribution of DXS-NPs at 24 hours following IV or IP-administration. Luciferase signal from tumor cells and infrared fluorescence from nanoparticles were measured for each organ using an IVIS instrument. Arrows denote metastases on organs. Most of the DXS-NP is scavenged by the liver following IV administration, but some NP co-localized heterogeneously with the primary tumor and intestinal metastases. More NP signal is detected from neoplastic tissues following IP-administration, including in metastases on the other IP organs.

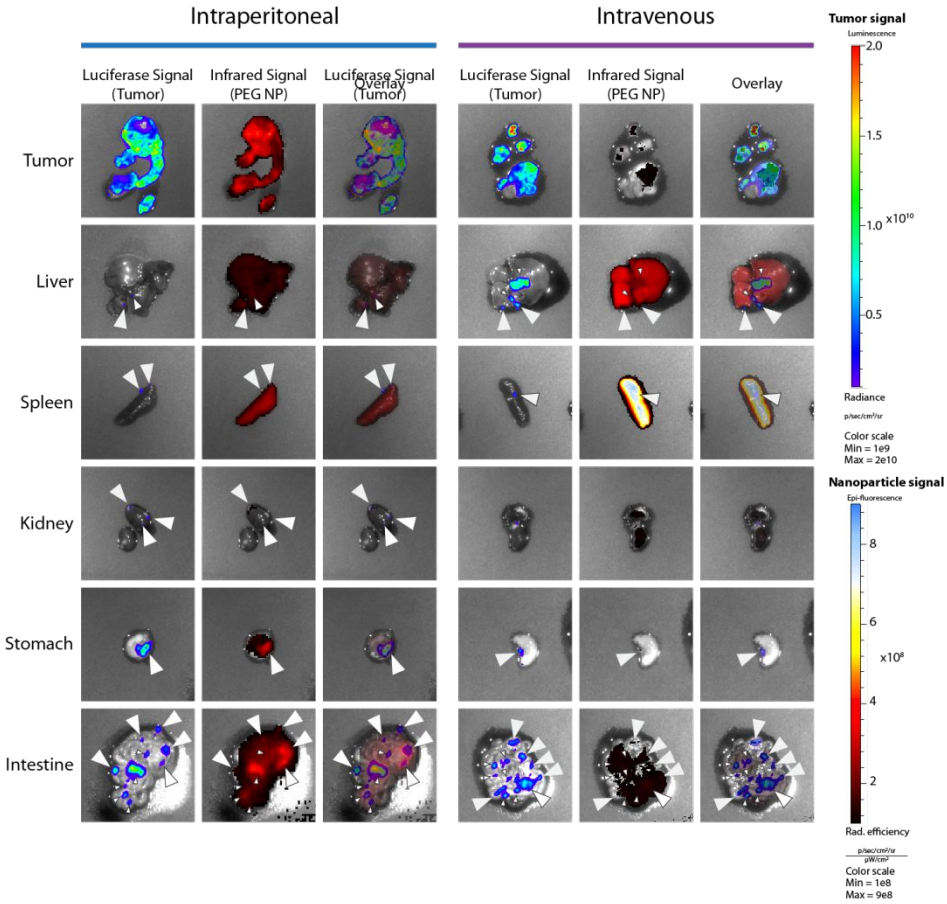

Figure S17. PEG-coated nanoparticle biodistribution at 24 hours following IP or IV administration. Luciferase signal from tumor cells and infrared fluorescence from nanoparticles were measured for each organ using an IVIS instrument. Arrows denote metastases on organs. IV administration led to NP co-localizing heterogenously with the primary tumor, and intestinal metastases. The amount of NP accumulating in tumors appears diminished in the IV-administration condition compared to the IP-administered condition. There is diffuse NP signal throughout the intestine that is not co-localized to tumor nodules. NP signal is detected throughout the liver and spleen for both IP and IV.

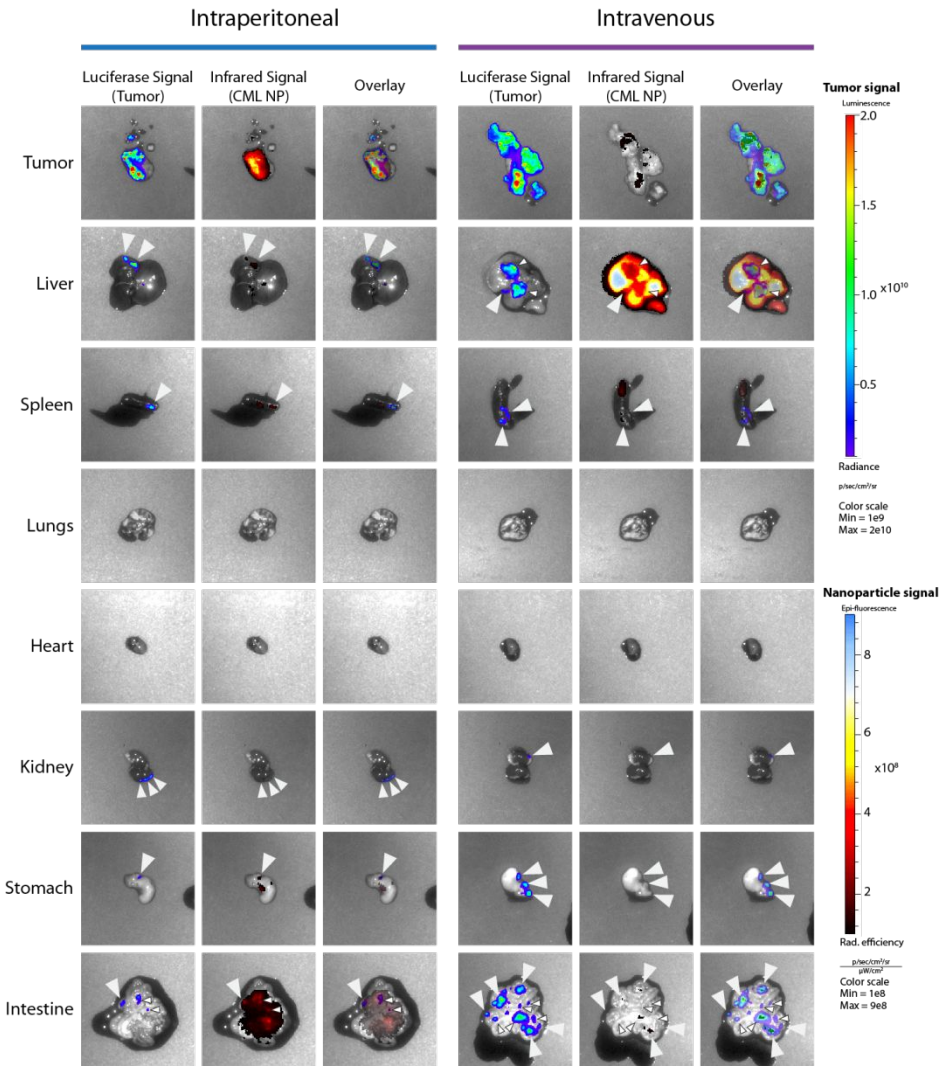

Figure S18. Representative images of the biodistribution of the unmodified CML-NP at 24 hours after either IV or IP-administration. Luciferase signal from tumor cells and infrared fluorescence from nanoparticles were measured for each organ using an IVIS instrument. Arrows denote metastases on organs. CML-NP co-localized with the primary tumor tissue when administered IP. NPs heterogeneously co-localize with the primary tumor and some intestinal metastasis following IV administration.

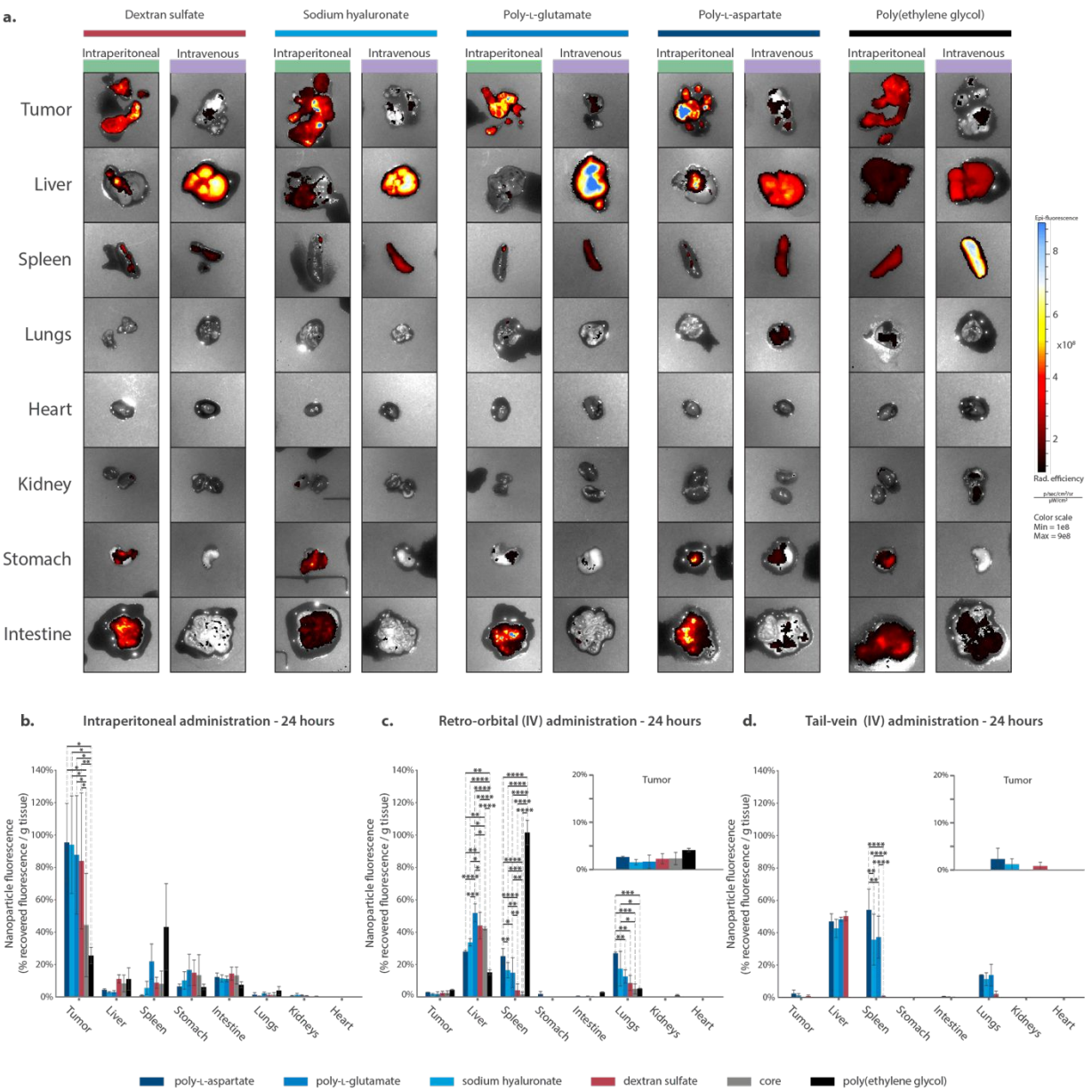

Figure S19. 24-hours after treatment, NP biodistribution is dominated by route of administration rather than surface chemistry. Infrared fluorescence from nanoparticles were measured for each organ using an IVIS instrument. (**a**) Retro-orbital IV administration are compared to IP-administration for PLD, PLE, HA, DXS, PEG, and CML-NPs. IV-administration skews NP biodistribution towards the liver and to a lesser extent the spleen. IP-administration skews NP distribution to neoplastic tissues in the IP cavity. (**b**) Quantification of the IVIS results reveals that LbL-NPs, but not CML-NPs, have a significant and improved accumulation in the primary tumor relative to PEGylated NPs. (**c**) Quantification of the results from retro-orbital IV injections indicate that surface chemistry may influence degree of accumulation in the liver, spleen, and lungs, but not accumulation in the tumor at this time point. (**d**) A smaller study comparing only LbL-

NPs was conducted using a tail-vein (TV) injection instead of retro-orbital injection. TV-administration led to undetectable PLE-NP signal in the tumors, but no significant differences for tumor accumulations observed with the other formulations. TV injection also reduced the amount of PLD NP delivered to the lungs. Other than this, the distribution to the liver and spleen remained consistent with retro-orbital injection. Error bars represent SEM. Multiple comparisons were performed using the FDR approach (Q= 5%) following 2-way ANOVA. Asterisks denote discoveries by FDR; **** $q < 0.0001$, *** $q < 0.001$, ** $q < 0.01$, * $q < 0.045$.

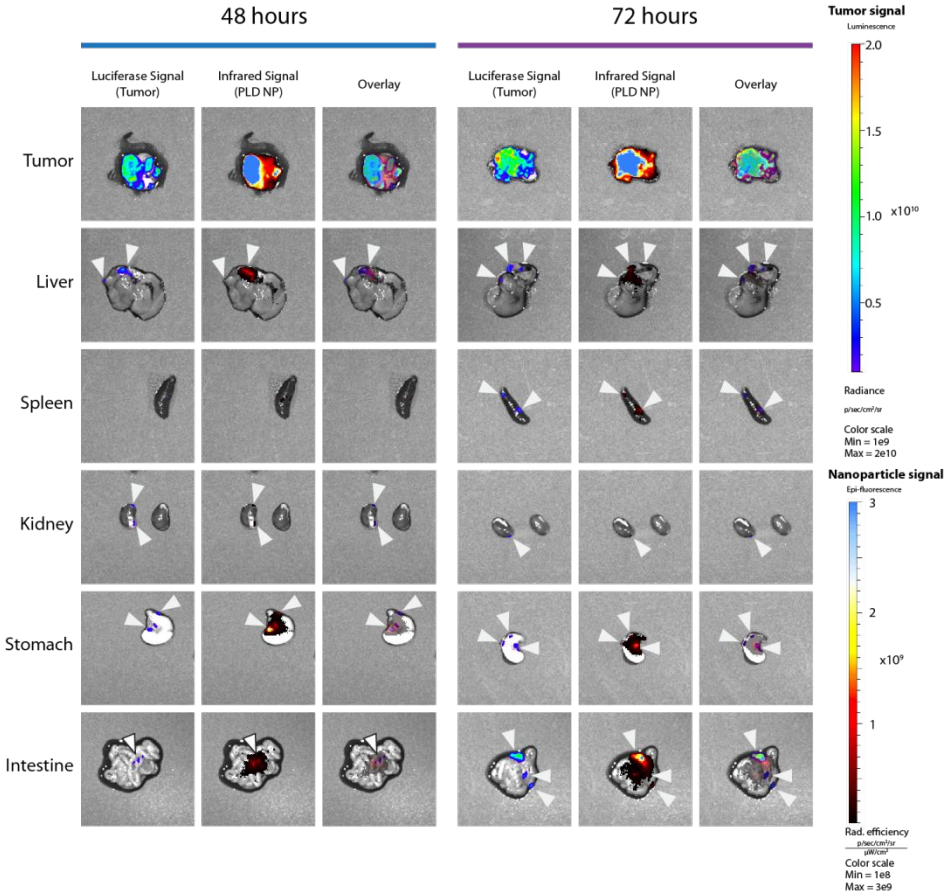

Figure S20. PLD-NP biodistribution at 48 and 72 hours following IP administration indicates sustained co-localization with neoplastic tissue. Luciferase signal from tumor cells and infrared fluorescence from nanoparticles were measured for each organ using an IVIS instrument. Arrows denote metastases on organs. PLD-coated NPs co-localize with the tumor bioluminescence.

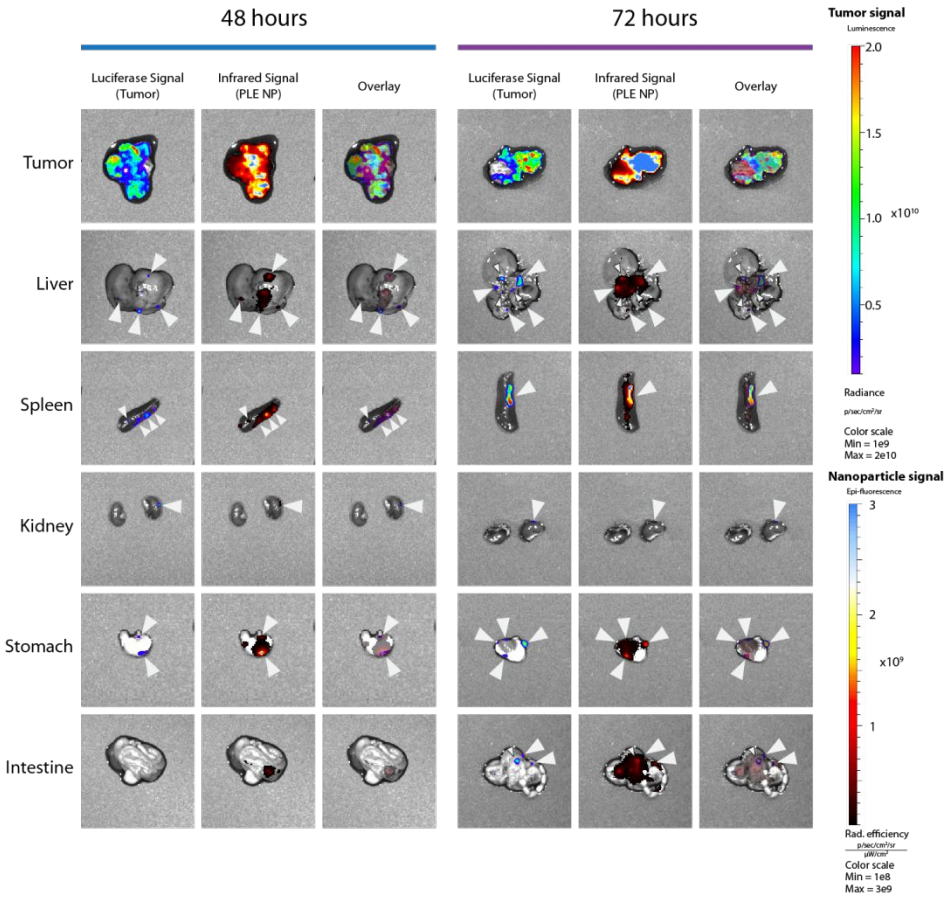

Figure S21. PLE-NP biodistribution at 48 and 72 hours following IP administration indicates sustained co-localization with neoplastic tissue. Luciferase signal from tumor cells and infrared fluorescence from nanoparticles were measured for each organ using an IVIS instrument. Arrows denote metastases on organs. Some diffuse NP signal in the intestines and stomach were not co-localized with detectable lesions, but the majority of signal appears to co-localize with tumor bioluminescence.

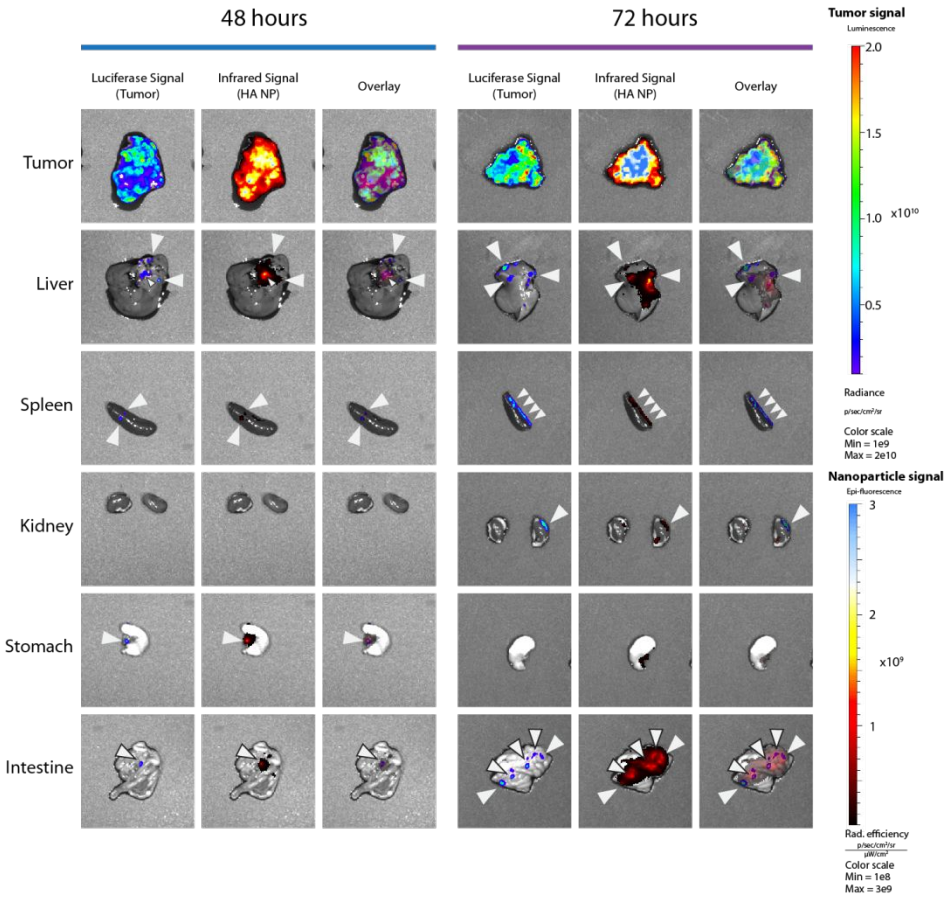

Figure S22. HA-NP biodistribution at 48 and 72 hours following IP administration indicates continued co-localization with neoplastic tissue. Luciferase signal from tumor cells and infrared fluorescence from nanoparticles were measured for each organ using an IVIS instrument. Arrows denote metastases on organs. Some diffuse NP signal in the intestines and stomach is not co-localized with detectable lesions, but the majority of signal appears to co-localize with tumor bioluminescence.

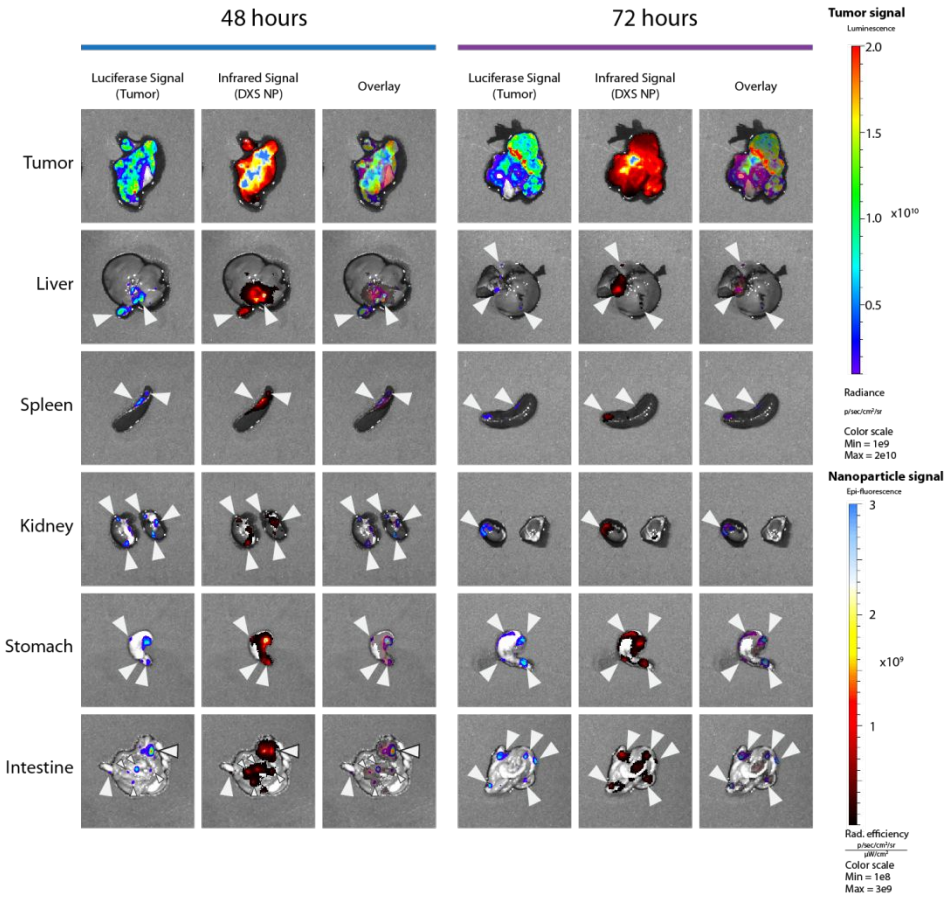

Figure S23. DXS-NP biodistribution at 48 and 72 hours following IP administration indicates decreasing co-localization with neoplastic tissue. Luciferase signal from tumor cells and infrared fluorescence from nanoparticles were measured for each organ using an IVIS instrument. Arrows denote metastases on organs. Signal from the primary tumor decreases from 48 to 72 hours.

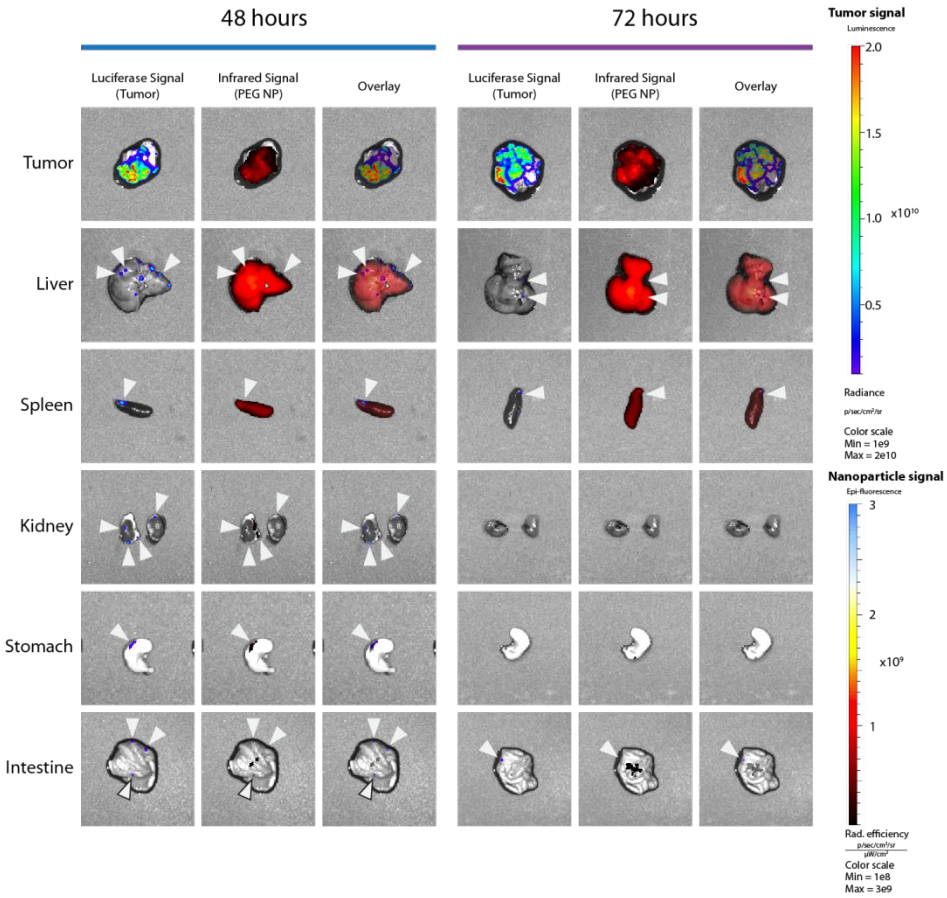

Figure S24. Biodistribution of PEGylated CML cores at 48 and 72 hours following IP administration indicates spillover of NP into the liver and spleen compartments. Luciferase signal from tumor cells and infrared fluorescence from nanoparticles were measured for each organ using an IVIS instrument. Arrows denote metastases on organs. PEG NPs had reduced co-localization with metastatic lesions at these times. NP signal increased in the liver and spleen over time.